









## Magnetic Reconnection During the Post-Impulsive Phase of a Long-Duration Solar Flare: Bi-Directional Outflows as a Cause of Microwave and X-ray Bursts

SIJIE YU (余思捷) <sup>1</sup>, BIN CHEN (陈彬) <sup>1</sup>, KATHARINE K. REEVES <sup>2</sup>, DALE E. GARY <sup>1</sup>, SOPHIE MUSSET <sup>3,4</sup>,  
GREGORY D. FLEISHMAN <sup>1</sup>, GELU M. NITA <sup>1</sup> AND LINDSAY GLESENER <sup>4</sup>

<sup>1</sup>*Center for Solar-Terrestrial Research, New Jersey Institute of Technology, 323 M L King Jr Blvd, Newark, NJ 07102-1982, USA*

<sup>2</sup>*Harvard-Smithsonian Center for Astrophysics, 60 Garden St, Cambridge, MA 02138, USA*

<sup>3</sup>*SUPA, School of Physics & Astronomy, University of Glasgow, Glasgow G12 8QQ, UK*

<sup>4</sup>*University of Minnesota, Minneapolis, MN, USA*

(Received TBD; Revised TBD; Accepted TBD)

Submitted to ApJ

### ABSTRACT

Magnetic reconnection plays a crucial role in powering solar flares, production of energetic particles, and plasma heating. However, where the magnetic reconnections occur, how and where the released magnetic energy is transported, and how it is converted to other forms remain unclear. Here we report recurring bi-directional plasma outflows located within a large-scale plasma sheet observed in extreme ultraviolet emission and scattered white light during the post-impulsive gradual phase of the X8.2 solar flare on 2017 September 10. Each of the bi-directional outflows originates in the plasma sheet from a discrete site, identified as a magnetic reconnection site. These reconnection sites reside at very low altitudes ( $< 180$  Mm, or  $0.26 R_{\odot}$ ) above the top of the flare arcade, a distance only  $< 3\%$  of the total length of a plasma sheet that extends to at least  $10 R_{\odot}$ . Each arrival of sunward outflows at the looptop region appears to coincide with an impulsive microwave and X-ray burst dominated by a hot source (10–20 MK) at the looptop, which is immediately followed by a nonthermal microwave burst located in the loopleg region. We propose that the reconnection outflows transport the magnetic energy released at localized magnetic reconnection sites outward in the form of kinetic energy flux and/or electromagnetic Poynting flux. The sunward-directed energy flux induces particle acceleration and plasma heating in the post-flare arcades, observed as the hot and nonthermal flare emissions.

**Keywords:** Solar flares (1496), Solar coronal mass ejections (310), nonthermal radiation sources (1119), Solar magnetic reconnection (1504), Solar radio flares (1342)

### 1. INTRODUCTION

The most powerful explosive phenomena in the solar system, solar flares accompanied by plasma eruptions, are powered by magnetic energy release in the solar corona facilitated by fast magnetic reconnection. In the standard CSHKP model of eruptive solar flares (Carmichael 1964; Sturrock 1966; Hirayama 1974; Kopp & Pneuman 1976), reconnection occurs in the diffusion region of a reconnection current sheet (RCS) formed in the wake of the eruption of a magnetic flux

rope. The latter, when observed by a coronagraph as a large-scale eruptive structure, is referred to as a coronal mass ejection (CME). At both sides of the RCS, magnetized plasma is drawn toward the RCS, where oppositely-directed magnetic fields reconnect, producing bi-directional plasma outflows along the RCS directed away from the reconnection site. Electrons and ions are accelerated at or in the close vicinity of the RCS to high energies (Masuda et al. 1994; Chen et al. 2018; Chen et al. 2020b; Fleishman et al. 2020). The downward propagating accelerated electrons arrive at the dense chromosphere and drive chromospheric evaporation. Hard X-ray (HXR) emission is produced at the footpoints of the newly reconnected magnetic loops

via bremsstrahlung. The dense chromospheric plasma heated to  $\sim 10$  MK is driven upward by the over-pressure and fills the flare arcade, which emits intense flare emission in extreme ultraviolet (EUV) and soft X-ray (SXR) wavelengths.

The magnetic reconnection is undoubtedly needed to drive the magnetic energy release. The released energy is converted to other forms of energy—bulk flows, heated plasma, and accelerated particles (see, e.g., a review by Benz 2017). Observational signatures of magnetic reconnection include *X*-shaped (Su et al. 2013; Sun et al. 2015; Zhu et al. 2016) or *Y*-shaped (Shibata et al. 2007) magnetic field lines, fan-spine-type structures (Liu et al. 2009; Zeng et al. 2016), supra-arcade fan or outflows (McKenzie & Hudson 1999; Savage et al. 2010; Savage & McKenzie 2011; Reeves et al. 2017), and large-scale thin plasma-sheet-like structures (Reeves & Golub 2011; Savage et al. 2012; Warren et al. 2018; Cheng et al. 2018; Longcope et al. 2018; Chen et al. 2020b). However, details of the magnetic reconnection, the associated energy release, and its conversion have yet to be clarified.

Bi-directional plasma outflows help in probing the magnetic reconnection. The sunward (downward) reconnection outflows usually exhibit as supra-arcade plasma downflows or fast-contracting loops in EUV and SXR data (Forbes & Acton 1996; Reeves et al. 2008; Liu et al. 2013; Takasao et al. 2012; McKenzie & Hudson 1999). Anti-sunward (upward) outflows have also been reported trailing the erupting flux rope (Nishizuka et al. 2010; Chae et al. 2017; Cheng et al. 2018). Occasionally, both the upward and downward plasma outflows are observed simultaneously (Savage et al. 2010; Takasao et al. 2012; Liu et al. 2013), which allows pinpointing the reconnection site. A similar pinpointing of the reconnection site with a very high positional accuracy (of  $< 1$  Mm) has been achieved by Chen et al. (2018) using radio imaging spectroscopy observations of decimetric type III radio bursts.

These plasma outflows carry a significant energy in the form of bulk kinetic energy flux, enthalpy flux, and electromagnetic Poynting flux (Fletcher & Hudson 2008; Birn et al. 2009). To convert these energy forms into that of accelerated particles and heated flare plasma, various mechanisms have been proposed involving turbulence or plasma waves (Hamilton & Petrosian 1992; Miller et al. 1996; Petrosian & Liu 2004; Liu et al. 2008, 2013; Fleishman & Toptygin 2013; Fleishman et al. 2020), fast-mode termination shocks (Forbes 1986; Masuda et al. 1994; Tsuneta & Naito 1998; Guo & Gialalone 2012; Nishizuka & Shibata 2013; Takasao et al. 2015; Chen et al. 2015, 2019; Shen et al. 2018; Kong et al. 2019), collapsing magnetic traps formed by fast-

contracting post-reconnection loops (Somov & Kosugi 1997; Karlický & Kosugi 2004; Giuliani et al. 2005; Karlický & Bárta 2006; Grady et al. 2012), magnetic islands (Drake et al. 2006; Oka et al. 2010), or Fermi-type acceleration from plasma compression (Li et al. 2018).

Occasionally, HXR sources are observed at or above the top of bright EUV/SXR flare arcades (Masuda et al. 1994; Veronig et al. 2006; Krucker et al. 2008a,b, 2010; Liu et al. 2013; Krucker & Battaglia 2014; Dennis et al. 2018). They have been regarded as an important piece of evidence of electron acceleration in the above-the-looptop (ALT) region. Recently, microwave imaging spectroscopy data from the Expanded Owens Valley Solar Array (EOVSA) have offered unprecedented spatially- and temporally-resolved measurements of non-thermal electrons and magnetic field in the flaring region (Gary et al. 2018). In particular, Fleishman et al. (2020) reported a fast decay of magnetic field in the ALT region. Further, Chen et al. (2020b) found that this region coincides with a local minimum of magnetic field strength, referred to as a “magnetic bottle”, where microwave-emitting, mildly relativistic electrons are highly concentrated. These observations imply that the ALT region, where plasma outflows interact vigorously with the underlying flare arcade, plays a crucial role in magnetic energy release and electron acceleration. Reported temporal correlation between the outflows and impulsive X-ray and/or radio emission (Asai et al. 2004; Karlický & Bárta 2007; Nishizuka et al. 2010; Chen et al. 2015; Takasao et al. 2016) further supports the role of the plasma outflows.

In this study, we report well-connected signatures of magnetic reconnection, plasma heating, and electron acceleration observed during the post-impulsive gradual phase of the X8.2-class eruptive solar flare on 2017 September 10. The combined white light and EUV imaging observations allow us to identify the timing and location of multiple intermittent reconnection events by bi-directional plasma outflows in an extremely long plasma sheet. The arrivals of the plasma downflows at the looptop correlate with plasma heating events that manifest as impulsive X-ray bursts. In the meantime, nonthermal microwave bursts, obtained by EOVSA, are detected in the loopleg region, which have no response in *RHESSI* hard X-rays. Such a chain of reconnection-associated observational signatures offers a new view of the energy release and conversion processes with a level of clarity not previously achieved.

In Section 2.1, we present imaging spectroscopy observations of impulsive microwave and X-ray bursts in the flare looptop and arcade (Section 2.2). In Section 2.3, we examine the microwave and X-ray bursts using spec-

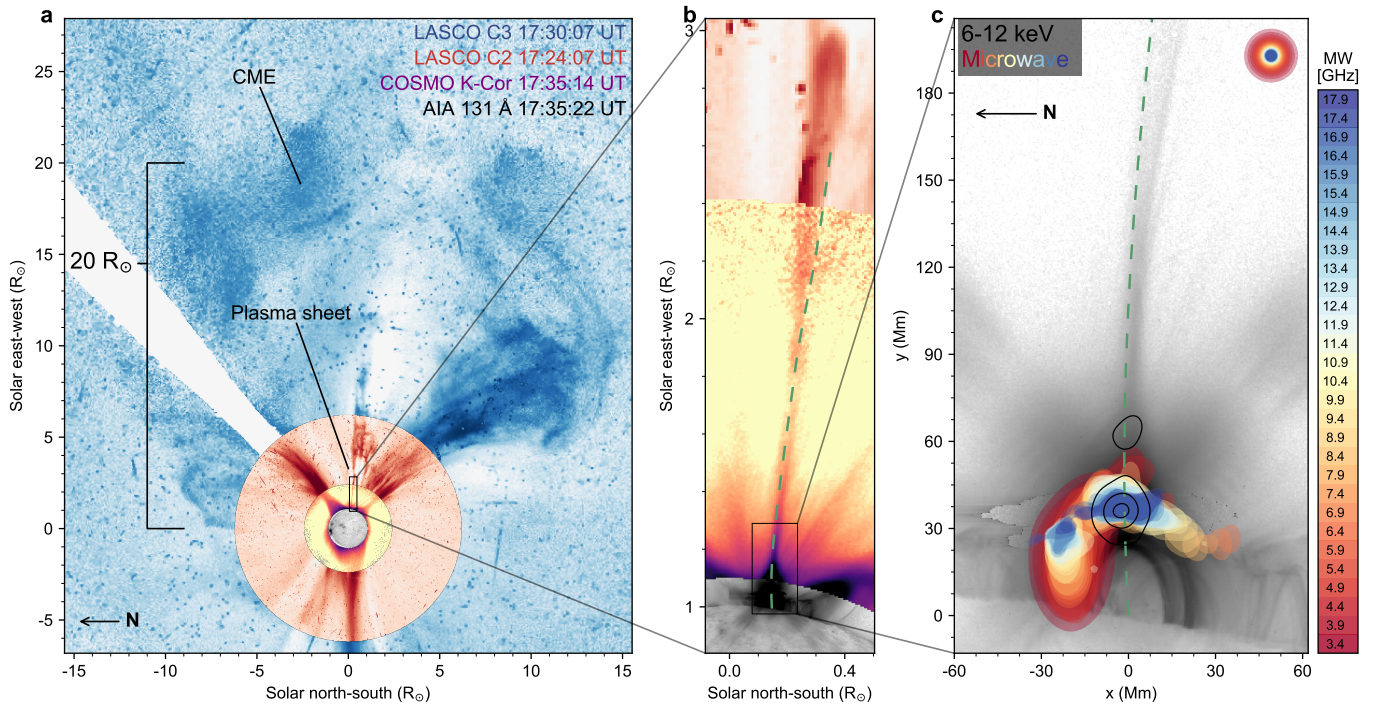


**Figure 1.** (a) Composition of the *SDO*/AIA 131 Å, *MLSO*/K-cor, *SOHO*/LASCO C2 and C3 white light images, showing the CME bubble and a long plasma sheet connecting the core of CME and the underlying flare site. All images are in reversed grayscale of log intensity, and rotated counter-clockwise by 90°. (b) Detailed view of the lower portion of the plasma sheet (black box in (a)) seen in EUV and white light. The green dashed curved is used to derive the time-distance maps shown in Fig. 7. (c) Further enlarged view of the low-coronal portion of the plasma sheet and the flare arcade (black box in (b)). The *EOVSA* microwave emission at 30 spectral windows is displayed as filled contours (25% of the respective maximum intensity), color-coded in frequency according to the colorbar. The filled circles on the upper right corner represent the full-width-half-maximum size of the restoring beams at the respective frequencies. *RHESSI* 6-12 keV X-ray source is superposed as black contours (10%, 50%, 90% of the maximum).

tral analysis. In Section 2.4, we present the detection of multitudes of bi-directional plasma outflows using white light and EUV imaging data that appear to correlate with the microwave and X-ray bursts. We discuss the implications of the observational results in Section 3, particularly on the role of the plasma outflows in energy transport and conversion.

## 2. OBSERVATIONS

The long-duration X8.2-class eruptive flare occurred close to the west solar limb on 2017 September 10. The event is associated with a fast white-light coronal mass ejection (CME), which has a speed of  $> 4000 \text{ km s}^{-1}$  (Gopalswamy et al. 2018) and is accompanied with a type II radio burst (Morosan et al. 2019). The eruption is well observed in microwaves by *EOVSA* (Gary et al. 2018) in 2.5–18 GHz, in EUV by the Atmospheric Imaging Assembly on board the Solar Dynamics Observatory (*SDO*/AIA; Lemen et al. 2012) and Solar Ultraviolet Imager on board the NOAA GOES-R satellite (Seaton & Darnel 2018), in white-light by

the COSMO K-Coronagraph of the Mauna Loa Solar Observatory (*MLSO*/K-Cor; Elmore et al. 2003) and the Large Angle and Spectrometric Coronagraph Experiment on board the solar and heliospheric observatory (*SoHO*/LASCO; Brueckner et al. 1995), and in X-Rays by Reuven Ramaty High-Energy Solar Spectroscopic Imager (*RHESSI*; Lin et al. 2002) and the Gamma-ray Burst Monitor aboard the *Fermi* spacecraft (Fermi/GBM; Meegan et al. 2009).

The event began at  $\sim 15:35$  UT when a pre-existing filament started to erupt. After  $\sim 15:50$  UT, the erupting filament developed into a teardrop-shaped dark cavity as seen in *SDO*/AIA images (Yan et al. 2018; Veronig et al. 2018) and microwaves (Chen et al. 2020a). The acceleration of the flux rope peaked at around 15:54 UT (Veronig et al. 2018), which coincided with an early impulsive peak in microwaves and HXRs (Chen et al. 2020a). The main peak of the impulsive microwave/HXR emission occurred at around 16:00 UT (Gary et al. 2018; Fleishman et al. 2020). By 17:30 UT well into the decay phase of the event, the CME front has already propagated to



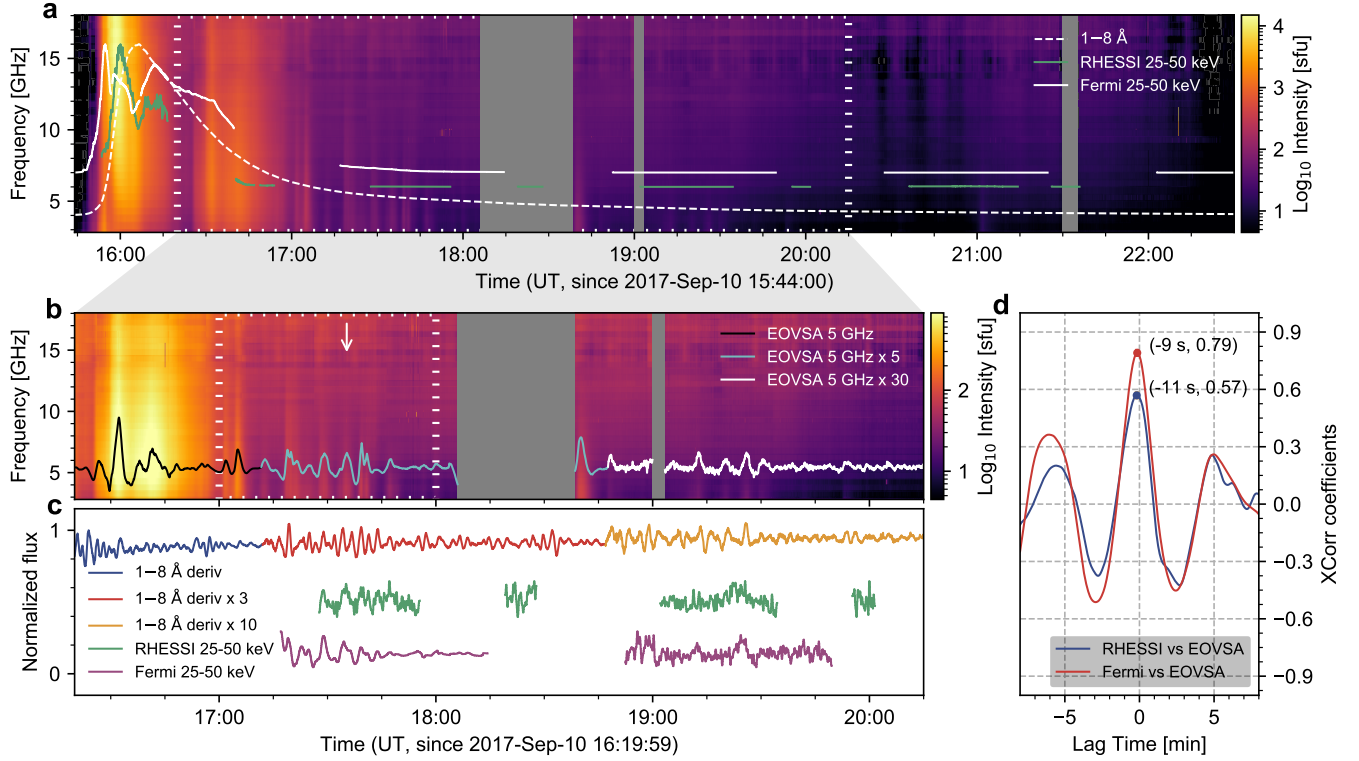


**Figure 2.** (a) *EOVSA* total-power (full-disk-integrated) microwave dynamic spectrum of the entire event in 2.5–18 GHz. Color presents the flux density in sfu. Overplotted are normalized time profiles of *GOES* 1–8 Å SXR (dashed curves), *RHESSI* and *Fermi* 25–50 keV HXR counts (solid green and white curves, respectively). (b) Enlarged *EOVSA* total-power dynamic spectrum of the post-impulsive phase. The time window is demarcated by a pair of vertical dashed lines in (a). Overplotted is the *EOVSA* 5 GHz light curve after removing the slowly-varying background. In order to aid visual comparison, the 5 GHz time profile between 17:12 and 18:47 UT and after 18:47 UT is multiplied by a factor of 5 and 30, respectively (shown in distinct colors). (c) Detrended light curves of *GOES* 1–8 Å time derivative, *RHESSI* and *Fermi* 25–50 keV HXR counts. The *GOES* derivative after 17:12 UT is amplified in a similar fashion to the *EOVSA* 5.0 GHz time profile in (b). (d) Cross-correlation between the *RHESSI*/*Fermi* 25–50 keV HXR and 5.0 GHz microwave light curves. The peak correlation coefficient occurs at –9 s and –11 s, respectively (HXR is ahead of microwave).

more than 20 solar radii ( $R_{\odot}$ ) above the solar surface (Figure 1(a)). A long and thin plasma sheet structure is present in the wake of the CME above the flare arcade (Figure 1; see also Yan et al. 2018; Warren et al. 2018; Longcope et al. 2018; Chen et al. 2020b), which extends into the SOHO/LASCO C3 field of view with a total length of at least  $8 R_{\odot}$  (Cheng et al. 2018; Lee et al. 2020). A *RHESSI* 6–12 keV X-ray source is present at the looptop region (open contours in Fig. 1c). No footpoint X-ray source is detected at this time.

### 2.1. Impulsive Microwave and X-ray Bursts

An overview of the long-duration event based on *EOVSA* and *RHESSI* data was provided by Gary et al. (2018). More detailed studies of the flux rope morphology, magnetic field variation along the RCS feature, and magnetic field decay during the initial and

main impulsive phase have been reported in our earlier publications (Chen et al. 2020a,b; Fleishman et al. 2020). In this study, we focus on the post-impulsive, long-duration gradual phase between 16:20 and 20:15 UT (Fig. 2(b)), shortly after the main impulsive phase at  $\sim 16:00$  UT (c.f., Fig. 2(a), when the brightest microwave emission of over 10,000 solar flux unit, or sfu, is present). During this period, the *EOVSA* total-power (full-disk integrated) microwave dynamic spectrum contains multiple broadband bursts. These bursts have an impulsive appearance in the dynamic spectrum and light curves. The relative amplitudes of the bursts at 5 GHz, represented as the ratio of the peak brightness of each burst to the pre- and post-burst background  $I_{\text{pk}}/I_{\text{bkg}}$ , is between 1.5%–30% (solid curves in Fig. 2(b)). These bursts have an average duration of  $\sim 4$  minutes and an average recurrence period of  $\sim 5.6$  minutes. The in-

dividual microwave bursts correlate with weak X-ray bursts at 6–100 keV observed by both *RHESSI* and *Fermi/GBM* (Fig. 2(c)). The X-ray bursts, however, have very small amplitudes of only a few percent and can only be distinguished in the detrended light curves, after the slow-varying background has been removed. For simplicity, we display only the 25–50 keV light curves, because the detrended light curves at different energies in 6–100 keV during the decay phase show very similar temporal behaviour and no time lag is found among them. Cross-correlation between the microwave and X-ray light curves indicate that the X-ray bursts lead the microwave bursts by  $\sim 10$  seconds (Fig. 2(d)). Some of the microwave bursts correspond to quasi-periodic impulsive peaks in the time derivative of the *GOES* 1–8 Å SXR light curve (Fig. 2(c)). The latter was reported in a recent paper by Hayes et al. (2019), who attributed these quasi-periodic features with a period of  $\sim 150$  seconds to magnetohydrodynamic (MHD) oscillations in the post-flare arcade.

## 2.2. X-ray spectroscopy and imaging

We analyze the *RHESSI* full-disk-integrated X-ray spectrum during the peak of a selected burst at around 17:35 UT integrated over a 28-s interval (indicated by a white arrow in Figure 2(b)) using the standard X-ray spectral analysis tool *OSPEX* available in the Solar-Soft Ware (SSW; Freeland & Handy 1998) IDL package. Ning et al. (2019) reported a significant pulse pileup effect on the *RHESSI* spectra in this event. Pileup results when two lower-energy photons arrive at the detector within a short time and are counted by the detector as a single higher-energy photon (Smith et al. 2002). We check the impact of the pulse pileup effect at  $\sim 17:35$  UT using the standard routine `hsi_pileup_check` in SSW. We find while pileup strongly affects the spectrum above  $\sim 20$  keV, the lower-energy range is almost pileup-free. Such pileup effect on relatively higher energies is also implied by the similar temporal behavior of the light curves between 6–100 keV (as mentioned in section 2.1), which is consistent with a dominant thermal plasma at lower energies and some pileup at higher energies. For mitigating the pileup effect, we restrict our spectral fit to only the low-energy range (6–25 keV). We also include the pileup in the detector response matrix for spectral fitting by adding the pileup module `pileup_mod` as a fitting component. Figure 3 shows the observed X-ray photon flux spectrum and the corresponding fit result. We found that the observed photon flux can be well fit by an isothermal model with a temperature of  $T = 20 \pm 0.2$  MK and a volume emission measure  $EM_V = 1.1 \pm 0.1 \times 10^{49} \text{ cm}^{-3}$  (red curve), together with

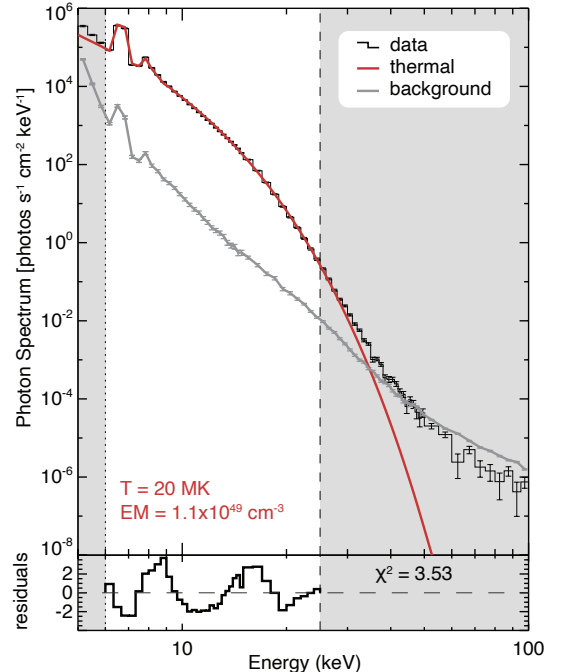


**Figure 3.** Example *RHESSI* HXR photon spectrum integrated between 17:34:44 UT and 17:35:12 UT after background subtraction (black histogram; background is shown in gray points). The fitted thermal component is shown in red curve. The normalized residuals vs. energy in units of the standard deviation of the count statistics are shown in the bottom panel. The gray shaded area indicates the energy range where the observed X-ray photon flux is excluded from the spectral fitting.

pulse pileup corrections. We note that, while the pileup effect at higher energies hinders us from constraining a possible nonthermal component based on the spectral fit, we cannot rule out the presence of a weak nonthermal component at the looptop region.

We reconstruct *RHESSI* X-ray images using the *CLEAN* algorithm (Hurford et al. 2002) with measurements from detectors 3, 6 and 8. Time-series images were made in three energy bands, 6–12 keV, 12–25 keV, and 25–50 keV, over two *RHESSI* observing windows in 17:28–17:55 UT and 19:02–19:35 UT with an integration time of 60 s for each individual image. Figure 4 shows an example of *RHESSI* images at the three energy bands. There is a persistent X-ray looptop source in 6–12 keV and 12–25 keV located near the apex of the flare arcade. Spectral analysis described above suggests that this source is dominated by thermal emission from a hot source with a temperature  $T \approx 20$  MK. The higher-energy 25–50 keV X-ray source appears co-spatial with the lower-energy source (Fig. 4(d)). However, this band is severely affected by the pileup effect (c.f., Fig. 3).

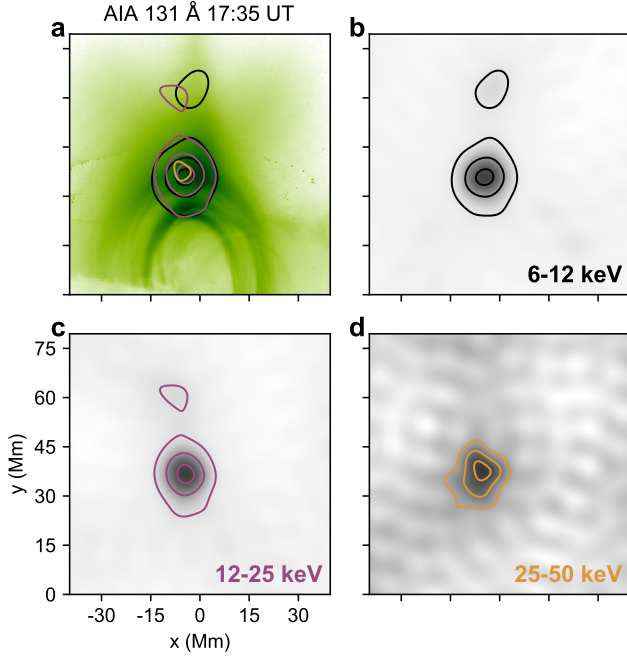


**Figure 4.** An example of *RHESSI* HXR images during the post-impulsive phase. (a) Contours of the 6–12 keV (black), 12–25 keV (green) and 25–50 keV (purple) sources on *SDO/AIA* 131 Å image at 17:35 UT with inverted color scale. The contour levels are 10%, 50% and 90% of the maximum for the 6–12 keV and 12–25 keV bands, and 90% of the maximum for the 25–50 keV band. (b–d) Same *RHESSI* images as in (a) shown separately. Note the 25–50 keV image is strongly affected by pulse pileup.

Thus we choose not to perform an in-depth analysis on the images of this band.

In the *RHESSI* 6–12 keV and 12–25 keV images, a weaker secondary coronal source is present above the primary source by  $\sim 27$  Mm. The secondary source is located near the tip of the cusp-shaped flare arcade, seen by *SDO/AIA* 131 Å (Fig. 4(a)), and is persistent over nearly the entire time of interest. Although its higher-energy counterpart is elusive due to the pileup effect, this secondary source appears reminiscent of the ALT HXR sources seen in the “Masuda-type” flares, where a HXR source is located slightly above the bright SXR/EUV flare arcade (Masuda et al. 1994; Veronig et al. 2006; Liu et al. 2013; Krucker & Battaglia 2014). We estimate the full width at half-maximum (FWHM) size of the primary and secondary source as  $\sim 11$  Mm and  $\sim 9$  Mm, respectively. Since the primary looptop source dominates the X-ray flux, we adopt its source

area to estimate an average column emission measure of  $\text{EM}_C \approx 2.9 \pm 0.3 \times 10^{30} \text{ cm}^{-5}$  in the looptop source<sup>1</sup>.

### 2.3. Microwave imaging spectroscopy

*EOVSA* provides microwave images in 2.5–18 GHz with 134 spectral channels spread over 31 spectral windows. In this work we combine each of the upper 30 spectral windows centered from 3.4 to 17.9 GHz to produce images at 30 equally spaced frequencies. Figure 1(c) shows the microwave images at these 30 frequencies at 17:35 UT (filled contours). The overall morphology of the evolving microwave source is consistent with the shape and orientation of the EUV flare arcade. At high frequencies (blue colors), there appear to be two distinct sources: one coincides with the looptop HXR source, while the other is in the northern leg of the flare arcade. At low frequencies, the microwave source concentrates in the northern leg of the flare arcade (on the left side in Fig. 1(c)), where the second (weaker) high-frequency microwave source is located. In contrast, microwave emission at all frequencies is weak or absent in the southern leg of the flare arcade (right side in the diagram).

The time-series of microwave images reveals that the impulsive component of the microwave emission in each burst is mainly from the loopleg source. Fig. 5(a–c) shows such time-sequence images for three selected microwave bursts peaking at 17:05 UT, 17:29 UT, and 17:35 UT, respectively (denoted as  $t_0$ ,  $t_1$ , and  $t_2$  in Fig. 5(f)). In these time-sequence images, the loopleg source shows a large variation in intensity during each burst (by a factor of up to 15). In contrast, the looptop source appears relatively stable with more-minor variations in morphology and intensity.

The dominance of loopleg brightening is better demonstrated in the *spatially-resolved*, or “vector”, dynamic spectra shown in Figs. 5(d–f). First introduced by Chen et al. (2015) using dynamic imaging spectroscopy data from the Karl G. Jansky Very Large Array (VLA), the technique of vector dynamic spectra takes advantage of the spatially, spectrally, and temporally resolved data to derive a radio dynamic spectrum for each selected region of interest in the spatial domain. This spatial separation allows the study of the temporal and spectral properties intrinsic to each radio source of interest. Here we select the looptop and loopleg sources

<sup>1</sup> It should be noted that the source area in the CLEAN images characterized by its full-width-half-maximum size may result in a slight overestimation (Kontar et al. 2010) and should be treated as the upper limit. However, the true source size should not be more than 10–20% smaller, and will not strongly affect our order-of-magnitude estimate of  $\text{EM}_C$  here.

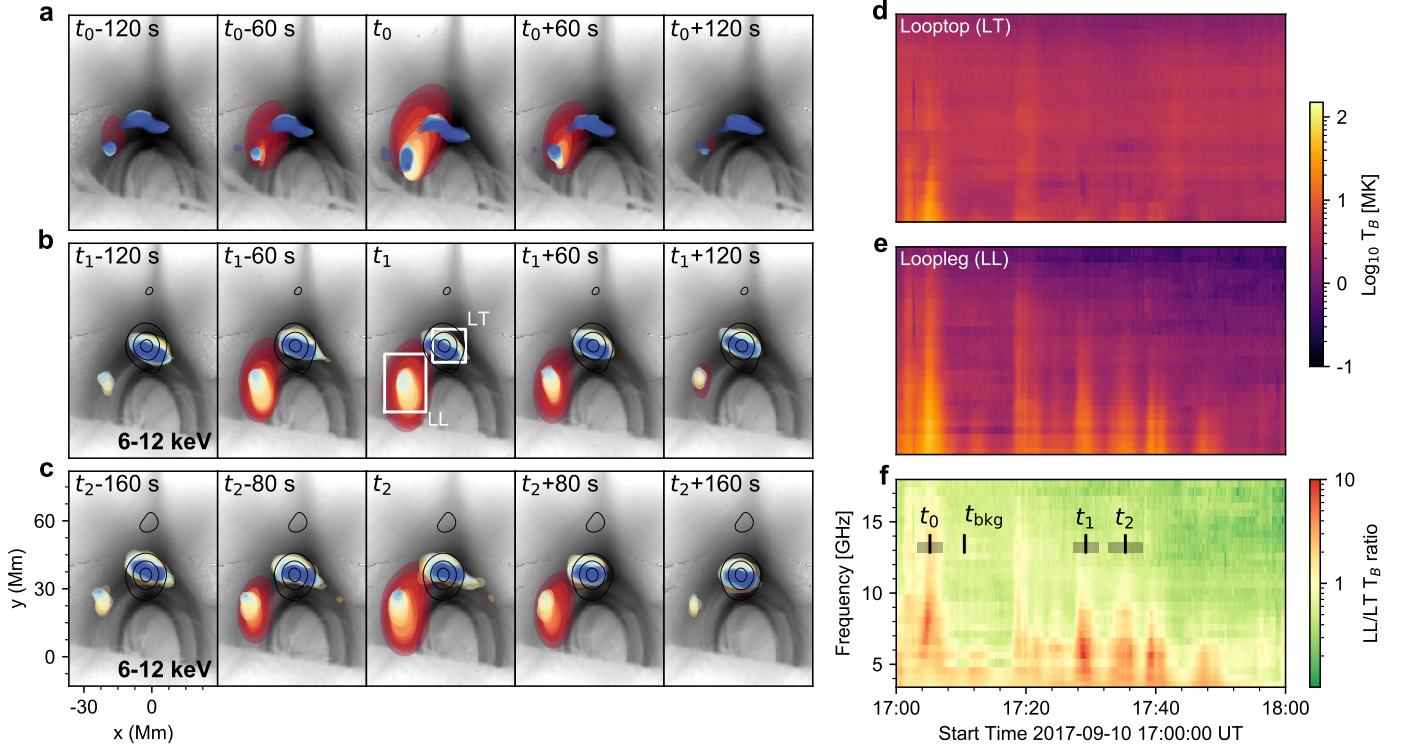


**Figure 5.** Spatial evolution of the microwave bursts observed by *EOVSA*. (a–c) Image sequences of the microwave emission (filled contours at 45% of the maximum brightness temperature of all images in the selected time interval; color represents different frequencies with same hue as in Figure 1(c)) overlaid on *SDO/AIA* 131 Å images during three time intervals. *RHESSI* 6–12 keV 15%, 50%, 90% contours are also superposed as black contours. The corresponding time  $t_0$ ,  $t_1$  and  $t_2$ , and the relevant time intervals are marked by the black vertical bars and the shaded stripes, respectively, in panel (f). (d) and (e) *EOVSA* spatially-resolved (vector) dynamic spectra derived from looptop and loopleg source from 17:00 UT to 18:00 UT, as well as their intensity ratio (f). The time range of the dynamic spectra is demarcated by the vertical dashed lines in Figure 2b.

(shown as the white boxes in Fig. 5(a)) and derive the maximum brightness temperature  $T_B$  within each box as a function of time and frequency. The resulting vector dynamic spectra for the loopleg and looptop source are shown in Fig. 5(d) and (e), respectively, and their intensity ratio is shown in Fig. 5(f). Although the loopleg and looptop source both display impulsive features, the bursts in the loopleg source are up to 10 times stronger than the looptop source (c.f., ratio spectrum in Fig. 5(f)).

To investigate the looptop and loopleg emission, we derive the spatially-resolved microwave brightness temperature spectra  $T_B(\nu)$  obtained at different spatial locations. Figure 6(e) shows the background-subtracted  $T_B(\nu)$  spectra obtained from several selected locations along the flare arcade (white boxes in Fig. 6(a–d)) at 17:05 UT ( $t_0$  in Fig. 5), during the peak of one of the brightest microwave bursts (solid black curves in Fig. 6(e)). The background spectra  $T_B^{\text{bk}}(\nu)$ , shown as gray curves in Fig. 6(e), are obtained at a time just after this microwave burst, denoted as  $t_{\text{bkg}}$  in Fig. 5(f). At the lowest frequencies, the background  $T_B$  spectra fol-

low a power law with a slope close to  $-2$ , suggesting an optically-thin, bremsstrahlung origin (e.g., Dulk 1985). At higher frequencies, the spectra are more complex with a flat or rising  $T_B$  toward higher frequencies, which is suggestive of a nonthermal gyrosynchrotron contribution.

Fig. 6(e) shows the background-subtracted microwave spectra as solid black curves. The spectra in the loopleg region (boxes 3–6) show characteristics of gyrosynchrotron radiation due to nonthermal electrons gyrating in the coronal magnetic field (e.g., Dulk 1985). We adopt the method described in Fleishman et al. (2020) to fit the spectra using a gyrosynchrotron emission model from an isotropic and homogeneous nonthermal electron source with a power-law energy distribution. From the spectral fit, we obtain the magnetic field strength  $B$ , the power-law index of the electron energy distribution  $\delta$ , and the total number density of nonthermal electrons  $n_e^{\text{nth}}$  integrated above 100 keV. The robustness and confidence level of the fit parameters are evaluated using a Markov chain Monte Carlo (MCMC) method, described in detail in Chen et al. (2020b). The derived magnetic



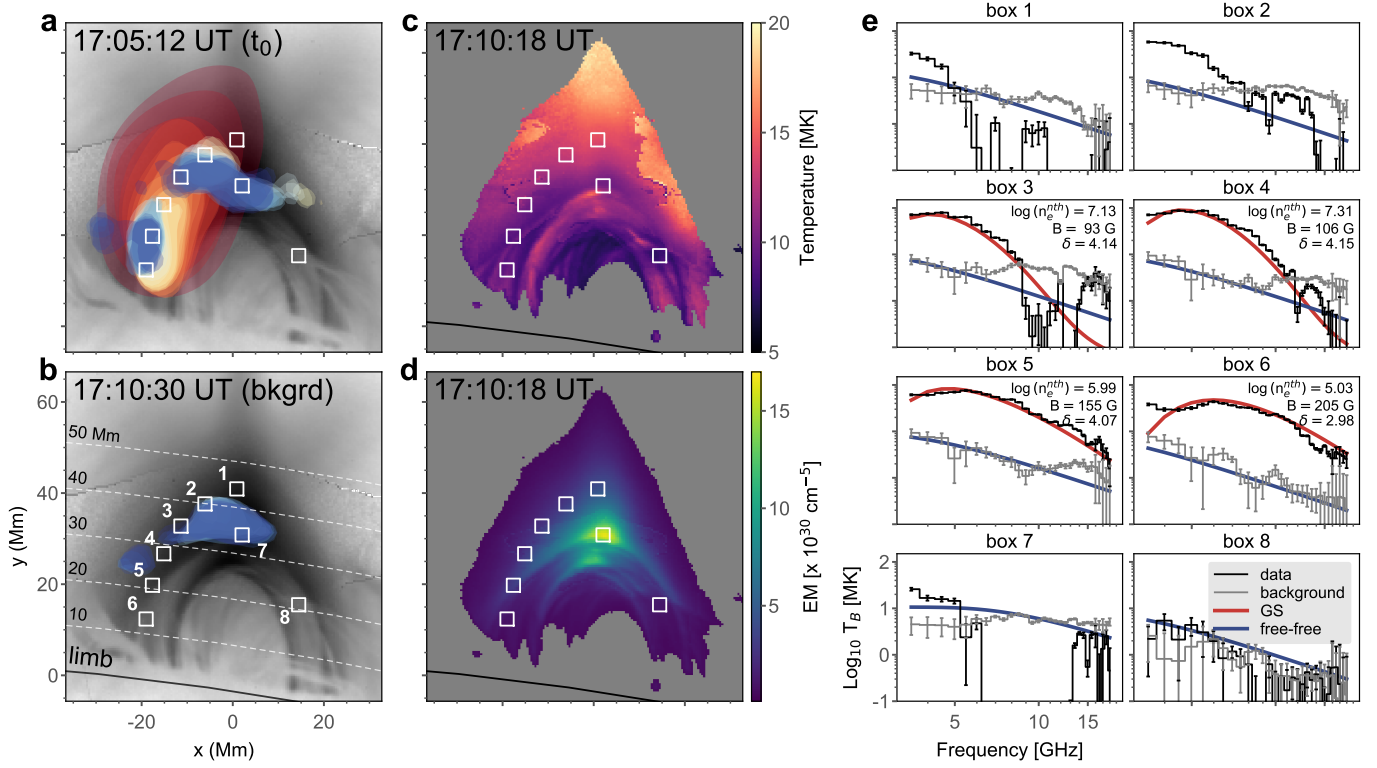


**Figure 6.** Spatially resolved microwave spectra at various points in the flare arcade. Enlarged view of the microwave burst (a) at  $t_0$  and (b) at a non-bursting time  $t_{bkg}$  selected as the background (filled contours at 30% of the maximum brightness temperature of all images at  $t_0$ ; same color scheme as in Figure 5(a)). (c) EM-weighted temperature and (d) integrated column emission measure  $EM_C$  maps obtained at  $t_{bkg}$  over the temperature range of 0.5–30 MK. (e) microwave brightness temperature spectra  $T_B(\nu)$  of the burst peak at  $t_0$  from eight selected locations (marked as numbered white boxes in (b)). The background-subtracted burst spectra and their corresponding background spectra derived at  $t_{bkg}$  are shown as black and gray histograms, respectively, with error bars. The observed emission at  $t_{bkg}$  is well matched by thermal free-free microwave spectra (blue lines) calculated using the AIA-derived DEM, while the burst enhancements in the loopleg source (boxes 3–6) are well fit by nonthermal gyrosynchrotron spectra (red lines) with the parameters shown in each plot.

field strength increases from 93 G to 205 G from box 3 to box 6, corresponding to height range from  $\sim 35$  Mm to  $\sim 15$  Mm. This is consistent with an expected increase of the magnetic field strength in a coronal loop towards lower heights. The values are also consistent with spectropolarimetric measurements of the magnetically sensitive Ca II 8542 Å line in the same post-arcade region about one hour before our time of interest (Kuridze et al. 2019). The power-law index of the electron energy distribution  $\delta$ , which ranges from 3.0–4.2, indicates a hardening toward lower heights (i.e., toward the loopleg region). The total number density of the nonthermal electrons  $n_e^{nth}$  above 100 keV is  $\sim 10^5$ – $10^7 \text{ cm}^{-3}$ , which is a small fraction of the thermal electron density in the same region (of order  $10^{10} \text{ cm}^{-3}$ , estimated based on the column emission measure shown in Fig. 6(d) and an assumed column depth of a few tens of Mm).

In the looptop region, however, the microwave spectra (except the lowest few frequencies) show very little

increment above the post-burst background (boxes 1, 2, and 7). The spectra (without background subtraction) are consistent with free-free (bremsstrahlung) radiation from hot thermal plasma with a temperature of 10–15 MK and column emission measure of  $2.9$ – $15.0 \times 10^{30} \text{ cm}^{-5}$  (blue curves in Fig. 6(e)). The latter is constrained using a differential emission measure (DEM) analysis method `xrt_dem_iterative2` (Weber et al. 2004; Golub et al. 2004) based on imaging data at six SDO/AIA EUV passbands (94 Å, 131 Å, 171 Å, 193 Å, 211 Å, and 335 Å). The microwave spectral and AIA DEM analysis of the looptop source is consistent with that derived from RHESSI (temperature of  $20 \pm 0.2$  MK and column emission measure of  $2.9 \pm 0.3 \times 10^{30} \text{ cm}^{-5}$ ; See section 2.2).

#### 2.4. Bi-directional outflows

Shortly after the eruption of the dark cavity at around 15:54 UT, a thin bright plasma sheet appeared in multiple SDO/AIA passbands, with a temperature of  $\sim 15$ –



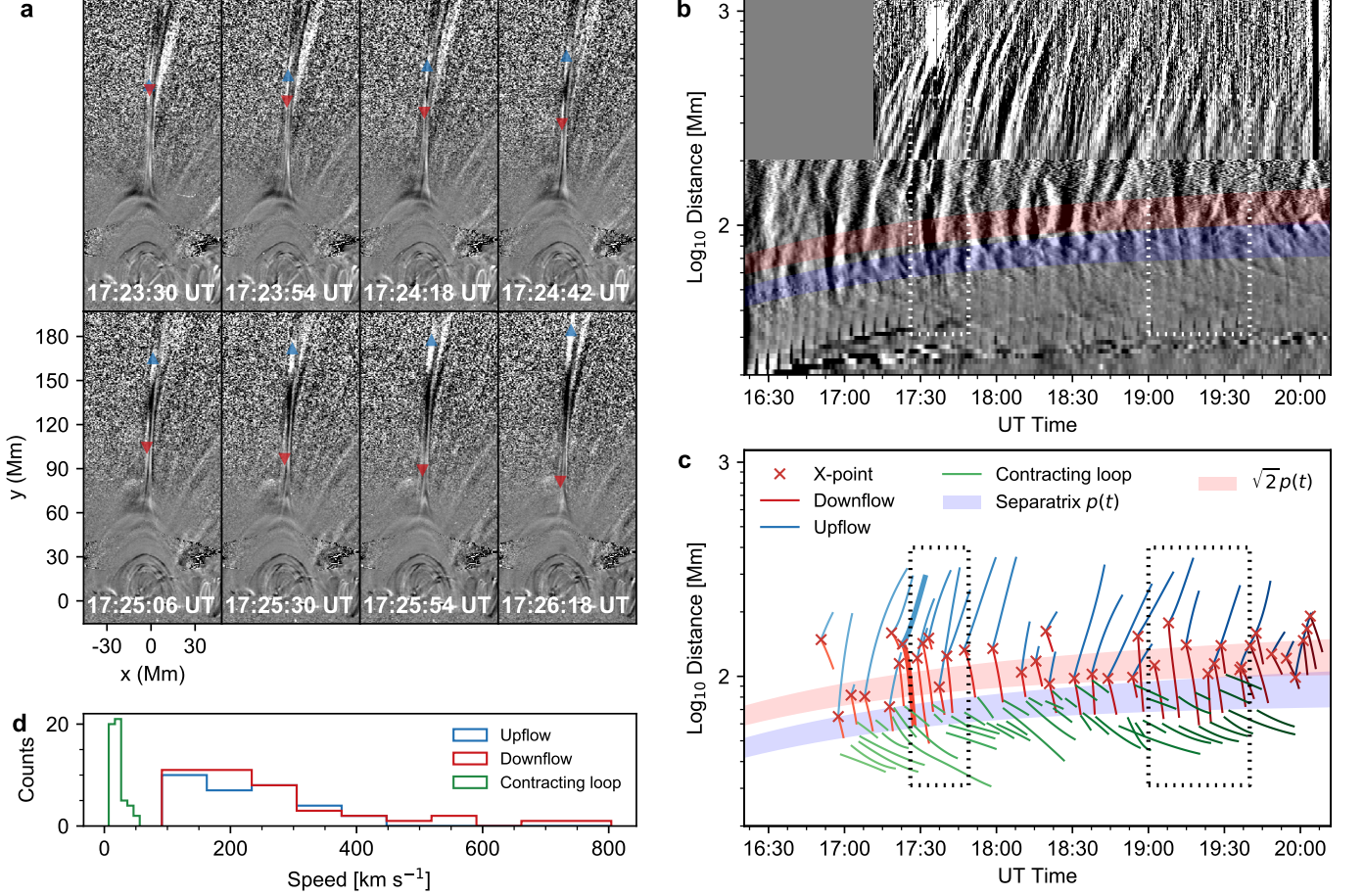


**Figure 7.** (a) Successive *SDO/AIA* 131 Å background-detrended images that show bi-directional outflows diverging from a compact region. The upward- and downward-moving EUV outflows are marked by red and blue triangles, respectively. Their tracks in the time-distance plot are highlighted as a pair of thick blue and red curves in (c). (b) Composite time-distance plot of *MLSO/K-cor* white light and *SDO/AIA* 131 Å background-detrended images at a cut made along the RCS (green dashed curve in Figure 1(b) and (c)). The upper edge of the AIA field of view is at  $\sim 200$  Mm. The blue shaded region marks the separatrix region that divides the fast plasma downflows and the slow contracting loops. The red shaded region shows the predicted height of the reconnection X point based on the idealized 2D flare model in Forbes et al. (2018). Note the distance axis is in *logarithmic* scale. (c) Tracks of the fast upward/downward outflows (blue/red) and slow contracting loops (green) in the time-distance plot. The inferred X points from the diverging sites of the bi-directional outflows are highlighted by the red crosses. (d) Histogram of the distribution of the measured speeds (in projection) of the plasma upflows (blue), plasma downflows (red), and contracting loops (green). An animation is available for the *SDO/AIA* 131 Å background-detrended images and its time-distance plot.

20 MK according to EUV spectroscopic data (Warren et al. 2018). In *SDO/AIA* 131 Å (which is sensitive to the Fe XXI line at  $\sim 10$  MK; O’Dwyer et al. 2010) images, multitudes of plasma outflows are present in the plasma sheet during different phases of the event for an extended period of time (Longcope et al. 2018; Cheng et al. 2018; Hayes et al. 2019; Chen et al. 2020b; Lee et al. 2020). Here we focus on the plasma outflows during the post-impulsive gradual phase from 16:20 UT to 20:20 UT. We find many recurring pairs of bi-directional plasma outflows that propagate simultaneously in the sunward (down) and anti-sunward (up) direction. A time sequence of one such outflow is shown in Fig. 7(a), in which

the slow-varying background is removed to enhance the dynamic features. The upward-moving EUV outflows extend well into the *MLSO/K-cor* field of view in white light to at least 1100 Mm (or  $1.6 R_{\odot}$ ) above the solar surface (Fig. 7(b)). The downward-moving EUV outflows seem to termination at the looptop region. Each pair of bi-directional outflows appears to diverge from a discrete site at varying heights in the plasma sheet.

To quantify the motion of the bi-directional plasma outflows, we construct a time-distance diagram from a slice along the direction of the plasma sheet feature seen in both *SDO/AIA* 131 Å and *MLSO/K-cor* images (green dashed curve in Figs. 1(b) and (c)). The

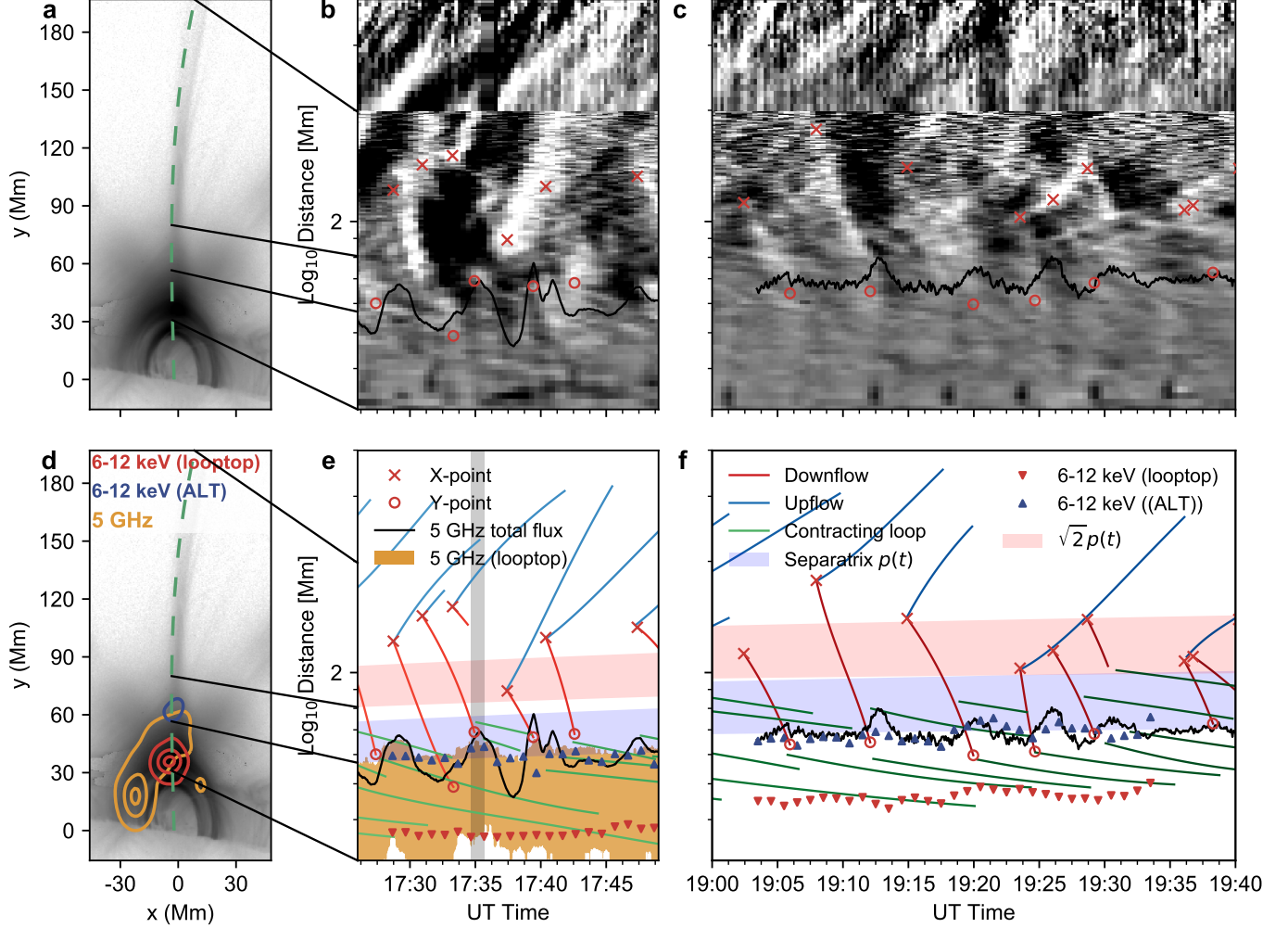


**Figure 8.** (a) *SDO/AIA* 131 Å image at 17:35 UT and the cut (same as the cut in Figure 1(b&c)). (b–c) Enlarged view of the time-distance plot for two selected time intervals shown as the white dashed boxes in Figure 7(b). The possible X- and Y-point are denoted by cross and circle. The black solid line is the detrended *EOVSA* 5 GHz light curve (same as the one shown in Figure 1(c)) superposed on the separatrix region that divides the fast downflows from the slow contracting loops. (d) Same as (a), but overlaid with 10%, 50%, and 90% contours of the 5 GHz microwave source (yellow) and 6–12 keV X-ray looptop source (red) and the weaker ALT X-ray source (blue). (e) and (f) Tracks of outflows (blue and red) and contracting loops (green) in the time-distance plots above. Also shown are the centroid locations of the looptop (red triangles) and ALT (blue triangles) X-ray sources, and the height range enclosed by the 10% contour of the 5 GHz microwave source (orange). The timing of the 6–12 keV X-ray and 5 GHz microwave images shown in (d) are indicated by the gray-shaded vertical stripe in (e).

slice has a width  $w_0 = 3$  Mm at the base. To improve the signal to noise at larger coronal distances, we increase the width of the slice linearly with distance  $d$  as  $w(d) = w_0 + 0.04d$ . At each time  $t$ , for every distance  $d$  along the slice, all pixels across the slice within width  $w$  are averaged to produce the intensity shown in the composite time-distance plot  $I(t, d)$ . The plasma upflows seen in EUV continue smoothly to the white light image seen at the upper edge of the *SDO/AIA* field of view at  $d \approx 200$  Mm (Fig. 7(b)). We selected the most prominent tracks and fitted either straight lines or basis

spline curves (de Boor 1972) to the projected height as a function of time. We identified 40 pairs of such bi-directional outflow tracks in 16:20–20:20 UT. There are also a few additional cases of downflow tracks without an obvious upward counterpart. As shown in the histogram of Fig. 7(d), the initial speeds of the upflows and downflows in projection are distributed between 100–800  $\text{km s}^{-1}$  with an average of 250  $\text{km s}^{-1}$ . These measured outflow speeds are consistent with previous reports of outflows in the same event (Cheng et al. 2018; Longcope et al. 2018; Hayes et al. 2019), and are typical for

SADs and SADLs reported in other events (McKenzie & Hudson 1999; Asai et al. 2004; McKenzie & Savage 2009; Savage & McKenzie 2011; Takasao et al. 2012; Liu et al. 2013). Similar to the interpretation adopted in previous studies (Savage et al. 2010; Takasao et al. 2012; Liu et al. 2013), we attribute the diverging location of each bi-directional outflow pair as the site of an individual magnetic reconnection event (or reconnection “X” point). Most of these identified reconnection sites are located at  $d \approx 50\text{--}180$  Mm (or  $0.07\text{--}0.26 R_{\odot}$ ) above the limb, which is only 1%–3% of the total length of the plasma sheet ( $\sim 10 R_{\odot}$ ) during that period.

The downflows fade away as they merge into the tip of the cusp-shaped flare arcade (sometimes referred to as the “Y” point; Priest & Forbes 2000; Chen et al. 2020b), where numerous slow, downward-contracting loops are present (see the animation accompanying Fig. 7). The slow contracting loops are also visible in the time-distance plots in Fig. 7(b) as multiple faint, finer tracks that branch off from the faster downflow tracks. Their initial speeds, measured using the slopes of the green lines in the time-distance plots, are only  $\sim 10\text{ km s}^{-1}$  or below. Such slow loop shrinkage is persistent throughout the gradual phase with an average recurrence period of  $\sim 3.2$  minutes. Although there is no one-to-one correspondence between the fast plasma downflows and the slow contracting motion of the post-reconnection flare loops, the slow-contracting loops appear in the close vicinity of the region where the fast downflows fade away, suggesting the presence of a “separatrix” region where the downflow motions appear to “terminate”.

The location of this separatrix region between the downflows and the contracting loops nearly coincides with the tip of the cusp-shaped flare arcade, shown as the blue colored shading in Figure 7(b–c). The lower edge of the separatrix region follows the end points of the fast downflow tracks. The upper edge follows the initial points of the slow contracting loop tracks. This separatrix region rises slowly during the gradual phase (blue shaded region in Figure 8(e–f)) in a similar fashion as the slow rise motion of the underlying microwave and X-ray looptop source located at the top of the flare arcade (red triangles in Figure 8(e–f); see also Gary et al. 2018; Hayes et al. 2019). The centroids of the ALT 6–12 keV X-ray source (blue triangles in Figure 8(e–f)), interestingly, are located near the separatrix region and follow the same rising motion. Possible implications of such a spatial-temporal coincidence will be discussed in the next section.

To illustrate the timing of the impulsive microwave bursts in accordance with the observed EUV plasma downflows, we overlay the *EOVSA* 5 GHz microwave

light curve (from Figure 1(c)) on the time–distance plots in Figure 8 near the separatrix region. The arrival of most EUV plasma downflows at the separatrix region is immediately followed by a microwave burst. This correlation in both space and time is a strong indication for a casual connection between the plasma downflows arriving at the looptop and the appearance of microwave-emitting nonthermal electrons in the flare arcade.

### 2.5. Summary of the Observations

1. Reconnection sites (or “X” points), from where the bi-directional plasma outflows diverge, reside at low altitudes  $< 180$  Mm, which are  $\sim 1\text{--}3\%$  of the total length of the long plasma sheet, which extends to  $> 10 R_{\odot}$ .
2. The arrival of most plasma downflows at the top of the cusp-shaped flare arcade correlates with an impulsive microwave and X-ray burst, which consists of a (mostly) thermal looptop microwave and X-ray source and a nonthermal loopleg microwave source. The loopleg microwave nonthermal source lags the looptop X-ray burst by  $\sim 10$  seconds.
3. Multitudes of slow contracting loops are present below the tip of the cusp-shaped flare arcade where the fast plasma downflows terminate. A secondary ALT X-ray source coincides with the separatrix region that divides the fast downflows and slow contracting loops.

## 3. DISCUSSION AND CONCLUSION

Our observational results are consistent with the standard CSHKP eruptive flare scenario for the post-impulsive phase (or gradual phase). At this stage, the eruption has already propagated to a remote coronal distance, leaving behind a large-scale vertical RCS above the post-flare arcade (see, e.g., Forbes et al. 2018). Figure 9(a) shows a schematic diagram for the post-impulsive phase projected in 2D adapted from a well-known cartoon in Forbes & Acton 1996. In this cartoon, the RCS and the underlying flare arcade are viewed edge on, in accordance with the viewing perspective of this event. Sporadic magnetic reconnections occur at localized magnetic null points (or X points) in the RCS, creating pairs of highly bent magnetic flux tubes (Furth et al. 1963). Plasma is ejected from the X points both upward and downward along the RCS, resulting in bi-directional plasma outflows.

The reconnection sites, pinpointed by the bi-directional plasma outflows, are located very low in the RCS. The heights of the X points are  $\sim 1\text{--}3\%$  of the total length of the RCS seen in EUV and white light,



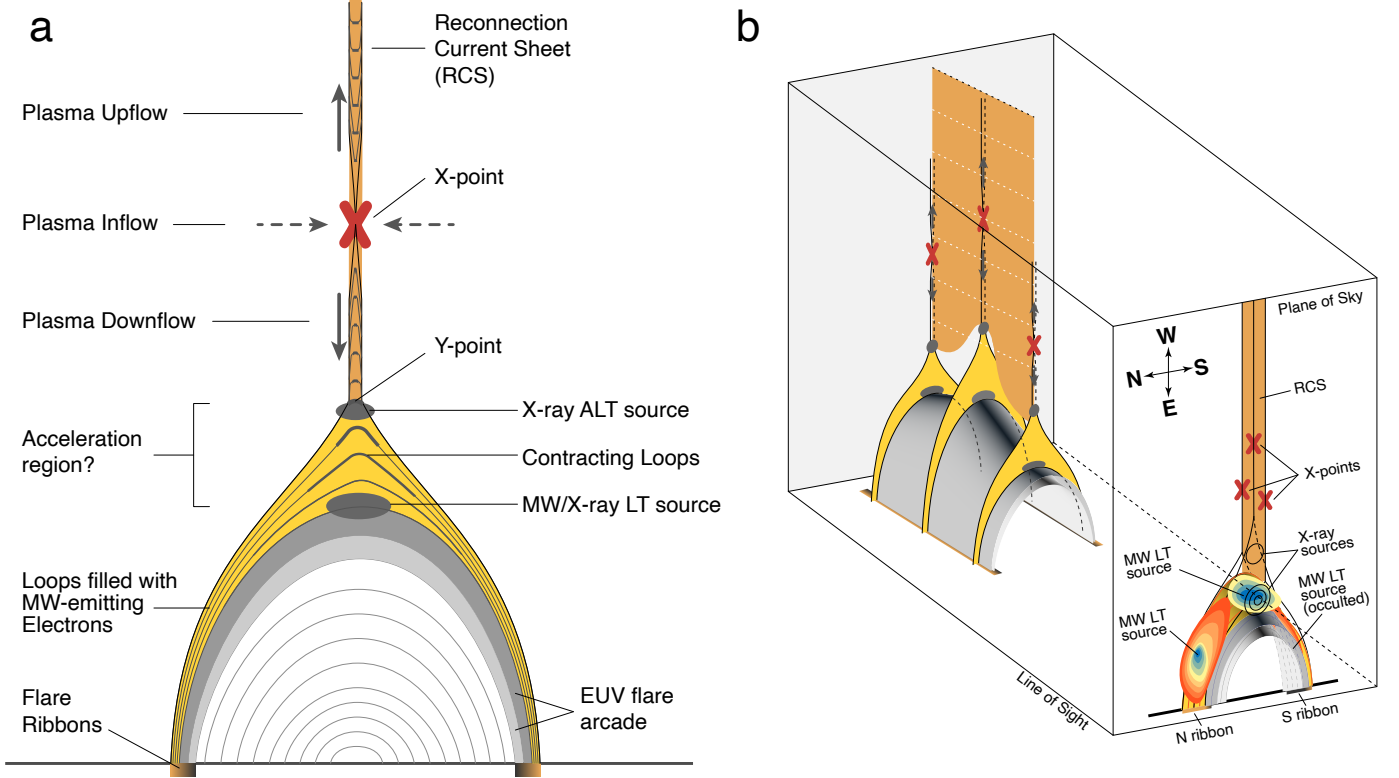


**Figure 9.** (a) Schematic diagram of post-impulsive flare arcade and the large-scale reconnection current sheet with an edge-on view (adapted from Forbes & Acton (1996)). Reconnection at multiple X points within the RCS results in a pair of highly-bent flux tubes that shrink quickly in both the sunward and anti-sunward directions, observed as the EUV plasma outflows. A microwave and X-ray source appears at the looptop due to plasma heating. Accelerated electrons in the flare arcade give rise to the nonthermal loopleg microwave source. A weak X-ray source is present near the Y point at the bottom of the RCS, where the fast downflows turn into slow contracting loops. The flare arcade itself is visible as a bright EUV arcade consisting of many strands. (b) Schematic diagram of flare arcade and the RCS depicted in 3D. Discrete reconnection events occur at different times and heights within the 3D RCS, visible as the observed scattering of the reconnection sites viewed edge on. Schematic of the observational signatures including the plasma sheet (with a finite width), EUV flare arcade, as well as microwave and X-ray sources are shown projected on the plane of sky. Here we adopt the possible interpretation in which the flare arcade may be slightly tilted with respect to the line of sight, which may account for the absence of the microwave source in the southern (right) side of the arcade.

which extends to at least  $10 R_{\odot}$ . The observed low reconnection sites within a long RCS are in agreement with predictions in the 2D theoretical model by Forbes et al. (2018), the latest development based upon one of most well-known standard flare models in Lin & Forbes (2000), Reeves & Forbes (2005) and Seaton & Forbes (2009). The 2D theoretical model predicts the height of the X point of approximately  $\sqrt{2}p(t)$  during the post-impulsive phase, where  $p(t)$  is the height of the Y point at the lower end of the RCS at time  $t$ . The latter marks the location where a thin RCS turns into a cusp-shaped post-reconnection flare arcade, measured as the tip of cusp loops seen in *SDO/AIA* 131 Å time-series images. As discussed in the previous section, this location also coincides with the separatrix region where the fast downflows, identified in the thin plasma sheet, meet the slow-contracting cusp loops below the cusp tip. In Figs. 7 and

8, we show the estimated location of the rising Y point as the blue shaded region and, according to the prediction in Forbes et al. (2018), the presumed location of the reconnection X point  $\sqrt{2}p(t)$  as the red shaded region. The predicted X point in idealized 2D flare model and its evolution in time agree with the location of the reconnection events pinpointed by the bi-directional plasma outflows in the thin plasma sheet. The scatter of the observationally-inferred reconnection sites around the model-predicted X point location is likely due to a deviation of the actual reconnection events from the idealized 2D model, together with the 3D nature of the flare event with multiple reconnection events distributed within the extended RCS along the direction of the LOS (illustrated in Fig. 9(b)).

In the 2D reconnection theories, the speeds of the reconnection outflows are at the local Alfvén speed (Sweet



1958; Parker 1957; Petschek & Thorne 1967). However, similar to many other reports (Savage et al. 2010; Savage & McKenzie 2011; Longcope et al. 2018; Hayes et al. 2019; Chen et al. 2020b), in our observations, the speeds of the bi-directional plasma outflows are between 100–800 km s<sup>-1</sup> with an average of 250 km s<sup>-1</sup>, which are likely sub-Alfvénic. It has been suggested that the observed plasma outflows may be sub-Alfvénic due to 3D effects, or have been slowed down as they emerge from the reconnection diffusion region by, e.g., an aerodynamic drag force (Longcope et al. 2018).

The plasma outflows carry a significant portion of the total released magnetic energy in the form of electromagnetic Poynting flux, enthalpy flux, and kinetic energy flux of the bulk flows or turbulence (Fletcher & Hudson 2008; Birn et al. 2009; Reeves et al. 2010; Warren et al. 2018; Cheng et al. 2018; Polito et al. 2018). Arrival of the downward-propagating plasma outflows at the cusp region dissipates their energy, resulting in plasma heating through thermal conduction and/or adiabatic heating (see, e.g., recent 3D modeling results in Reeves et al. 2019). If a fast-mode termination shock is established in the cusp region (which is perhaps implicated by the presence of the secondary ALT X-ray source near the cusp tip), plasma heating would occur in the shock downstream region (Forbes 1986; Masuda et al. 1994). Such heated plasma is revealed by the thermal X-ray and microwave source observed at the looptop.

The impulsively released magnetic energy during the sporadic magnetic reconnection events in the RCS can also lead to particle acceleration. Electrons can be accelerated to nonthermal energies in the RCS, at the looptop, or in the flare arcade itself by a variety of acceleration mechanisms (see, e.g., Miller et al. 1997 for a review). In our observations, the nonthermal microwave bursts only occur in the loopleg region at a large distance away from the reconnection X points. Considering the electron transport effects, the non-detection of nonthermal sources within the RCS is inconclusive to judge if the RCS is the electron acceleration site (see also Chen et al. 2020b). Nevertheless, HXR and microwave imaging spectroscopy data (Krucker et al. 2010; Krucker & Battaglia 2014; Fleishman et al. 2020; Chen et al. 2020b) have provided increasing evidence favoring the looptops/cusp regions as the primary electron acceleration sites.

In our event, the cusp region as the primary plasma heating and electron acceleration site is supported by the relative timing between the X-ray/microwave bursts and the magnetic reconnection events in the RCS (inferred from the occurrence of the bi-directional outflows). An important clue, as shown in Fig. 8, is that the occurrence

of the X-ray/microwave bursts correlates with the *arrival* time of the plasma downflows at the cusp, but not the time of the magnetic reconnection events themselves. A straightforward interpretation is that the electrons responsible for the microwave bursts are accelerated locally at the looptops, where freshly injected energy is available from the arrival of the plasma downflows. An alternative scenario is that the microwave-emitting electrons are accelerated in the RCS, but are trapped in the propagating plasma downflows. These electrons are released once the plasma downflows have arrived at the looptop, resulting in the nonthermal microwave sources. Although our data alone can not distinguish between the two scenarios, the latter scenario requires an additional mechanism that traps and/or accelerates the electrons within the plasma outflows along their path, while “breaks” this trapping upon the arrival of the outflows at the looptop.

The observed recurring bursts possess a recurrence period of  $\sim 300$  seconds and a modulation depth of 1.5% to 30% reminiscent of quasi-periodic pulsations (QPPs) observed in X-rays and microwaves during flares (Foullon et al. 2005; Mészáros et al. 2006; Reznikova & Shibasaki 2011). Such QPPs with long periods are sometimes referred to as *long* QPPs (Nakariakov & Melnikov 2009). One of the most intriguing questions about QPPs is what drives them during flares. The possible causes are generally categorized into two groups: (1) time-dependent energy release, and 2) MHD oscillations in flare sites (see Nakariakov & Melnikov 2009; McLaughlin et al. 2018, for reviews). Differentiating observationally between the possible explanations of long-period QPPs during flares remains elusive. The relative timing between X-ray/microwave bursts and the reconnection events we observe, however, allows for the determination of the origin of these particular bursts, although we leave open the question of whether they should be considered as QPPs. We find that the timing of the microwave and X-ray bursts is entirely driven by the reconnection at the X points, which rules out the MHD interpretation as the driver of the bursts. Nevertheless, Hayes et al. (2019) recently reported persistent QPPs with a two-times shorter period of  $\sim 150$  seconds in *GOES* SXR and *SDO/AIA* 131 Å light curves during the gradual phase of this same flare. The time-dependent magnetic reconnection mechanism we describe cannot fully account for these shorter-period QPPs, and other mechanisms such as MHD oscillations could play a role in modulating these lower-energy thermal emissions. As pointed out by Hayes et al. (2019), persistent QPPs require a renewed excitation of MHD modes in the flare arcade, and the recurring reconnection-generated downflows we

describe could provide the needed repetitive trigger at or above the the post-flare arcade (Takasao & Shibata 2016; Jelínek et al. 2017).

In our observation, the microwave bursts produced by mildly relativistic electrons ( $\gtrsim 100$  keV) in the loopleg region lag the thermal looptop X-ray bursts by  $\sim 10$  seconds. Such time delay has been reported by Bastian et al. (2007) between microwave and X-ray (tens of keV) event based on non-imaging light curves during a flare. Similar high-energy-delay phenomena have been reported in the literature—that high energy X-ray fluxes ( $\gtrsim 150$  keV) lagged behind their counterparts at lower energies by a few seconds in flares (Bai et al. 1983; Dulk et al. 1992). It has been suggested that such delays may be the result of a two-stage acceleration mechanism that invokes stochastic acceleration to boost electron energies from tens of keV to above hundreds of keV, assuming that this process requires a few second to operate (Dulk et al. 1992; Miller et al. 1997). Consequently, the high-energy electrons producing microwave emission appear later than the low-energy ones, so that the microwave bursts lag the thermal looptop X-ray bursts due to prompt plasma heating upon the arrivals of plasma outflows. Yet, the microwave and X-ray sources in this event are located at regions spatially separated by about 20 Mm. Hence the localized hardening of electron energy spectrum near the acceleration site at the looptop may not fully account for the time lag of the loopleg source. Electron transport and trapping effects should play a role in the time delay between the spatially separated sources.

In the ideal 2D standard model, the microwave source is expected to *bestride* the flare arcade. However, there is a marked asymmetry in the observed microwave emission in the post-flare arcade: a microwave source is only visible in the northern loopleg while the southern leg is not. One explanation could be due to the perspective effect that the event is tilted slightly away from the ideal 2D standard model projection, so that the microwave source at the southern leg of the flare arcade may be re-absorbed by optically-thick, dense plasma filled in

the arcade (perhaps due to chromospheric evaporation) located in the forefront along the LOS (illustrated in Fig. 9(b)). However, we could not completely rule out a coronal loop asymmetry as a possible cause of the dissimilar radio brightness of the northern and southern loop legs.

To summarize, thanks to the new microwave imaging spectroscopy observations from *EOVSA*, we have presented a comprehensive study that associates the bi-directional EUV plasma outflows in a large-scale RCS to looptop microwave and X-ray bursts in both time and space. The performed multi-wavelength analysis allowed us to quantify particle acceleration and plasma heating in the post-flare arcades, observed as the hot and non-thermal flare emissions, and their relationships with the magnetic reconnection in the RCS. Our findings reveal new facets of magnetic reconnection, the subsequent energy conversion, and electron acceleration, and thus help to better understand these fundamental phenomena.

#### ACKNOWLEDGMENTS

EOVSA operation is supported by NSF grant AST-1910354. S.Y., B.C. are supported by NSF grants AGS-1654382, AGS-1723436, and AST-1735405 to NJIT. K.R. is supported by NSF grant AGS-1923365 to SAO and grant 80NSSC18K0732 from NASA to SAO. G.F. and G.N. are supported by NSF grant AGS-1817277 and NASA grants 80NSSC18K0667, 80NSSC19K0068, 80NSSC18K1128, to New Jersey Institute of Technology. The work was supported partly by NASA DRIVE Science Center grant 80NSSC20K0627. We thank Dr. Chengcai Shen for his inspiring MHD modeling on solar flares. We thank the SDO/AIA team for providing the EUV data. We thank the *RHESSI* and *Fermi*-GBM team for providing the hard X-ray data. We also thank the *SoHO*/LASCO and *K-Cor* teams for providing white-light data.

*Facilities:* OVRO:SA, SDO, SoHO, K-Cor, RHESSI, Fermi

#### REFERENCES

- Asai, A., Yokoyama, T., Shimojo, M., & Shibata, K. 2004, ApJL, 605, L77, doi: [10.1086/420768](https://doi.org/10.1086/420768)
- Bai, T., Hudson, H. S., Pelling, R. M., et al. 1983, ApJ, 267, 433, doi: [10.1086/160881](https://doi.org/10.1086/160881)
- Bastian, T. S., Fleishman, G. D., & Gary, D. E. 2007, ApJ, 666, 1256, doi: [10.1086/520106](https://doi.org/10.1086/520106)
- Benz, A. O. 2017, Living Reviews in Solar Physics, 14, 2, doi: [10.1007/s41116-016-0004-3](https://doi.org/10.1007/s41116-016-0004-3)
- Birn, J., Fletcher, L., Hesse, M., & Neukirch, T. 2009, ApJ, 695, 1151, doi: [10.1088/0004-637X/695/2/1151](https://doi.org/10.1088/0004-637X/695/2/1151)
- Brueckner, G. E., Howard, R. A., Koomen, M. J., et al. 1995, SoPh, 162, 357, doi: [10.1007/BF00733434](https://doi.org/10.1007/BF00733434)
- Carmichael, H. 1964, A Process for Flares, Vol. 50, 451
- Chae, J., Cho, K., Kwon, R.-Y., & Lim, E.-K. 2017, ApJ, 841, 49, doi: [10.3847/1538-4357/aa6d7a](https://doi.org/10.3847/1538-4357/aa6d7a)

- Chen, B., Bastian, T. S., Shen, C., et al. 2015, *Science*, 350, 1238, doi: [10.1126/science.aac8467](https://doi.org/10.1126/science.aac8467)
- Chen, B., Shen, C., Reeves, K. K., Guo, F., & Yu, S. 2019, *ApJ*, 884, 63, doi: [10.3847/1538-4357/ab3c58](https://doi.org/10.3847/1538-4357/ab3c58)
- Chen, B., Yu, S., Reeves, K. K., & Gary, D. E. 2020a, under review
- Chen, B., Yu, S., Battaglia, M., et al. 2018, *ApJ*, 866, 62, doi: [10.3847/1538-4357/aadb89](https://doi.org/10.3847/1538-4357/aadb89)
- Chen, B., Shen, C., Gary, D. E., et al. 2020b, under review
- Cheng, X., Li, Y., Wan, L. F., et al. 2018, *ApJ*, 866, 64, doi: [10.3847/1538-4357/aadd16](https://doi.org/10.3847/1538-4357/aadd16)
- de Boor, C. 1972, *Journal of Approximation Theory*, 6, 50, doi: [https://doi.org/10.1016/0021-9045\(72\)90080-9](https://doi.org/10.1016/0021-9045(72)90080-9)
- Dennis, B. R., Duval-Poo, M. A., Piana, M., et al. 2018, *ApJ*, 867, 82, doi: [10.3847/1538-4357/aae0f5](https://doi.org/10.3847/1538-4357/aae0f5)
- Drake, J. F., Swisdak, M., Che, H., & Shay, M. A. 2006, *Nature*, 443, 553, doi: [10.1038/nature05116](https://doi.org/10.1038/nature05116)
- Dulk, G. A. 1985, *ARA&A*, 23, 169, doi: [10.1146/annurev.aa.23.090185.001125](https://doi.org/10.1146/annurev.aa.23.090185.001125)
- Dulk, G. A., Kiplinger, A. L., & Winglee, R. M. 1992, *ApJ*, 389, 756, doi: [10.1086/171248](https://doi.org/10.1086/171248)
- Elmore, D. F., Burkepile, J. T., Darnell, J. A., Lecinski, A. R., & Stanger, A. L. 2003, *Society of Photo-Optical Instrumentation Engineers (SPIE) Conference Series*, Vol. 4843, Calibration of a ground-based solar coronal polarimeter, ed. S. Fineschi, 66–75, doi: [10.1117/12.459279](https://doi.org/10.1117/12.459279)
- Fleishman, G. D., Gary, D. E., Chen, B., et al. 2020, *Science*, 367, 278, doi: [10.1126/science.aax6874](https://doi.org/10.1126/science.aax6874)
- Fleishman, G. D., & Toptygin, I. N. 2013, *MNRAS*, 429, 2515, doi: [10.1093/mnras/sts518](https://doi.org/10.1093/mnras/sts518)
- Fletcher, L., & Hudson, H. S. 2008, *ApJ*, 675, 1645, doi: [10.1086/527044](https://doi.org/10.1086/527044)
- Forbes, T. G. 1986, *ApJ*, 305, 553, doi: [10.1086/164268](https://doi.org/10.1086/164268)
- Forbes, T. G., & Acton, L. W. 1996, *ApJ*, 459, 330, doi: [10.1086/176896](https://doi.org/10.1086/176896)
- Forbes, T. G., Seaton, D. B., & Reeves, K. K. 2018, *ApJ*, 858, 70, doi: [10.3847/1538-4357/aabad4](https://doi.org/10.3847/1538-4357/aabad4)
- Foullon, C., Verwichte, E., Nakariakov, V. M., & Fletcher, L. 2005, *A&A*, 440, L59, doi: [10.1051/0004-6361:200500169](https://doi.org/10.1051/0004-6361:200500169)
- Freeland, S. L., & Handy, B. N. 1998, *SoPh*, 182, 497, doi: [10.1023/A:1005038224881](https://doi.org/10.1023/A:1005038224881)
- Furth, H. P., Killeen, J., & Rosenbluth, M. N. 1963, *Physics of Fluids*, 6, 459, doi: [10.1063/1.1706761](https://doi.org/10.1063/1.1706761)
- Gary, D. E., Chen, B., Dennis, B. R., et al. 2018, *ApJ*, 863, 83, doi: [10.3847/1538-4357/aad0ef](https://doi.org/10.3847/1538-4357/aad0ef)
- Giuliani, P., Neukirch, T., & Wood, P. 2005, *ApJ*, 635, 636, doi: [10.1086/497366](https://doi.org/10.1086/497366)
- Golub, L., Deluca, E. E., Sette, A., & Weber, M. 2004, in *Astronomical Society of the Pacific Conference Series*, Vol. 325, The Solar-B Mission and the Forefront of Solar Physics, ed. T. Sakurai & T. Sekii, 217–+
- Gopalswamy, N., Yashiro, S., Mäkelä, P., et al. 2018, *ApJL*, 863, L39, doi: [10.3847/2041-8213/aad86c](https://doi.org/10.3847/2041-8213/aad86c)
- Grady, K. J., Neukirch, T., & Giuliani, P. 2012, *A&A*, 546, A85, doi: [10.1051/0004-6361/201218914](https://doi.org/10.1051/0004-6361/201218914)
- Guo, F., & Giacalone, J. 2012, *ApJ*, 753, 28, doi: [10.1088/0004-637X/753/1/28](https://doi.org/10.1088/0004-637X/753/1/28)
- Hamilton, R. J., & Petrosian, V. 1992, *ApJ*, 398, 350, doi: [10.1086/171860](https://doi.org/10.1086/171860)
- Hayes, L. A., Gallagher, P. T., Dennis, B. R., et al. 2019, *ApJ*, 875, 33, doi: [10.3847/1538-4357/ab0ca3](https://doi.org/10.3847/1538-4357/ab0ca3)
- Hirayama, T. 1974, *SoPh*, 34, 323, doi: [10.1007/BF00153671](https://doi.org/10.1007/BF00153671)
- Hurford, G. J., Schmahl, E. J., Schwartz, R. A., et al. 2002, *SoPh*, 210, 61, doi: [10.1023/A:1022436213688](https://doi.org/10.1023/A:1022436213688)
- Jelínek, P., Karlický, M., Van Doorselaere, T., & Bárta, M. 2017, *ApJ*, 847, 98, doi: [10.3847/1538-4357/aa88a6](https://doi.org/10.3847/1538-4357/aa88a6)
- Karlický, M., & Bárta, M. 2006, *ApJ*, 647, 1472, doi: [10.1086/505460](https://doi.org/10.1086/505460)
- . 2007, *A&A*, 464, 735, doi: [10.1051/0004-6361:20065983](https://doi.org/10.1051/0004-6361:20065983)
- Karlický, M., & Kosugi, T. 2004, *A&A*, 419, 1159, doi: [10.1051/0004-6361:20034323](https://doi.org/10.1051/0004-6361:20034323)
- Kong, X., Guo, F., Shen, C., et al. 2019, *ApJL*, 887, L37, doi: [10.3847/2041-8213/ab5f67](https://doi.org/10.3847/2041-8213/ab5f67)
- Kontar, E. P., Hannah, I. G., Jeffrey, N. L. S., & Battaglia, M. 2010, *ApJ*, 717, 250, doi: [10.1088/0004-637X/717/1/250](https://doi.org/10.1088/0004-637X/717/1/250)
- Kopp, R. A., & Pneuman, G. W. 1976, *SoPh*, 50, 85, doi: [10.1007/BF00206193](https://doi.org/10.1007/BF00206193)
- Krucker, S., & Battaglia, M. 2014, *ApJ*, 780, 107, doi: [10.1088/0004-637X/780/1/107](https://doi.org/10.1088/0004-637X/780/1/107)
- Krucker, S., Hudson, H. S., Glesener, L., et al. 2010, *ApJ*, 714, 1108, doi: [10.1088/0004-637X/714/2/1108](https://doi.org/10.1088/0004-637X/714/2/1108)
- Krucker, S., Hurford, G. J., MacKinnon, A. L., Shih, A. Y., & Lin, R. P. 2008a, *ApJL*, 678, L63, doi: [10.1086/588381](https://doi.org/10.1086/588381)
- Krucker, S., Battaglia, M., Cargill, P. J., et al. 2008b, *A&A Rv*, 16, 155, doi: [10.1007/s00159-008-0014-9](https://doi.org/10.1007/s00159-008-0014-9)
- Kuridze, D., Mathioudakis, M., Morgan, H., et al. 2019, *ApJ*, 874, 126, doi: [10.3847/1538-4357/ab08e9](https://doi.org/10.3847/1538-4357/ab08e9)
- Lee, J.-O., Cho, K.-S., Lee, K.-S., et al. 2020, *ApJ*, 892, 129, doi: [10.3847/1538-4357/ab799a](https://doi.org/10.3847/1538-4357/ab799a)
- Lemen, J. R., Title, A. M., Akin, D. J., et al. 2012, *SoPh*, 275, 17, doi: [10.1007/s11207-011-9776-8](https://doi.org/10.1007/s11207-011-9776-8)
- Li, X., Guo, F., Li, H., & Li, S. 2018, *ApJ*, 866, 4, doi: [10.3847/1538-4357/aae07b](https://doi.org/10.3847/1538-4357/aae07b)
- Lin, J., & Forbes, T. G. 2000, *J. Geophys. Res.*, 105, 2375, doi: [10.1029/1999JA900477](https://doi.org/10.1029/1999JA900477)

- Lin, R. P., Dennis, B. R., Hurford, G. J., et al. 2002, *SoPh*, 210, 3, doi: [10.1023/A:1022428818870](https://doi.org/10.1023/A:1022428818870)
- Liu, W., Berger, T. E., Title, A. M., & Tarbell, T. D. 2009, *ApJL*, 707, L37, doi: [10.1088/0004-637X/707/1/L37](https://doi.org/10.1088/0004-637X/707/1/L37)
- Liu, W., Chen, Q., & Petrosian, V. 2013, *ApJ*, 767, 168, doi: [10.1088/0004-637X/767/2/168](https://doi.org/10.1088/0004-637X/767/2/168)
- Liu, W., Petrosian, V., Dennis, B. R., & Jiang, Y. W. 2008, *ApJ*, 676, 704, doi: [10.1086/527538](https://doi.org/10.1086/527538)
- Longcope, D., Unverferth, J., Klein, C., McCarthy, M., & Priest, E. 2018, *ApJ*, 868, 148, doi: [10.3847/1538-4357/aaeac4](https://doi.org/10.3847/1538-4357/aaeac4)
- Masuda, S., Kosugi, T., Hara, H., Tsuneta, S., & Ogawara, Y. 1994, *Nature*, 371, 495, doi: [10.1038/371495a0](https://doi.org/10.1038/371495a0)
- McKenzie, D. E., & Hudson, H. S. 1999, *ApJL*, 519, L93, doi: [10.1086/312110](https://doi.org/10.1086/312110)
- McKenzie, D. E., & Savage, S. L. 2009, *ApJ*, 697, 1569, doi: [10.1088/0004-637X/697/2/1569](https://doi.org/10.1088/0004-637X/697/2/1569)
- McLaughlin, J. A., Nakariakov, V. M., Dominique, M., Jelínek, P., & Takasao, S. 2018, *SSRv*, 214, 45, doi: [10.1007/s11214-018-0478-5](https://doi.org/10.1007/s11214-018-0478-5)
- Meegan, C., Lichti, G., Bhat, P. N., et al. 2009, *ApJ*, 702, 791, doi: [10.1088/0004-637X/702/1/791](https://doi.org/10.1088/0004-637X/702/1/791)
- Mészáros, H., Karlický, M., Rybák, J., Fárnik, F., & Jiříčka, K. 2006, *A&A*, 460, 865, doi: [10.1051/0004-6361:20065750](https://doi.org/10.1051/0004-6361:20065750)
- Miller, J. A., Larosa, T. N., & Moore, R. L. 1996, *ApJ*, 461, 445, doi: [10.1086/177072](https://doi.org/10.1086/177072)
- Miller, J. A., Cargill, P. J., Emslie, A. G., et al. 1997, *J. Geophys. Res.*, 102, 14631, doi: [10.1029/97JA00976](https://doi.org/10.1029/97JA00976)
- Morosan, D. E., Carley, E. P., Hayes, L. A., et al. 2019, *Nature Astronomy*, 3, 452, doi: [10.1038/s41550-019-0689-z](https://doi.org/10.1038/s41550-019-0689-z)
- Nakariakov, V. M., & Melnikov, V. F. 2009, *SSRv*, 149, 119, doi: [10.1007/s11214-009-9536-3](https://doi.org/10.1007/s11214-009-9536-3)
- Ning, H., Chen, Y., Lee, J., et al. 2019, *Research in Astronomy and Astrophysics*, 19, 173, doi: [10.1088/1674-4527/19/12/173](https://doi.org/10.1088/1674-4527/19/12/173)
- Nishizuka, N., & Shibata, K. 2013, *PhRvL*, 110, 051101, doi: [10.1103/PhysRevLett.110.051101](https://doi.org/10.1103/PhysRevLett.110.051101)
- Nishizuka, N., Takasaki, H., Asai, A., & Shibata, K. 2010, *ApJ*, 711, 1062, doi: [10.1088/0004-637X/711/2/1062](https://doi.org/10.1088/0004-637X/711/2/1062)
- O'Dwyer, B., Del Zanna, G., Mason, H. E., Weber, M. A., & Tripathi, D. 2010, *A&A*, 521, A21, doi: [10.1051/0004-6361/201014872](https://doi.org/10.1051/0004-6361/201014872)
- Oka, M., Phan, T. D., Krucker, S., Fujimoto, M., & Shinohara, I. 2010, *ApJ*, 714, 915, doi: [10.1088/0004-637X/714/1/915](https://doi.org/10.1088/0004-637X/714/1/915)
- Parker, E. N. 1957, *J. Geophys. Res.*, 62, 509, doi: [10.1029/JZ062i004p00509](https://doi.org/10.1029/JZ062i004p00509)
- Petrosian, V., & Liu, S. 2004, *ApJ*, 610, 550, doi: [10.1086/421486](https://doi.org/10.1086/421486)
- Petschek, H. E., & Thorne, R. M. 1967, *ApJ*, 147, 1157, doi: [10.1086/149105](https://doi.org/10.1086/149105)
- Polito, V., Dudík, J., Kašparová, J., et al. 2018, *ApJ*, 864, 63, doi: [10.3847/1538-4357/aad62d](https://doi.org/10.3847/1538-4357/aad62d)
- Priest, E., & Forbes, T. 2000, *Magnetic Reconnection: MHD Theory and Applications* (New York: Cambridge University Press), doi: [10.1017/CBO9780511525087](https://doi.org/10.1017/CBO9780511525087)
- Reeves, K. K., & Forbes, T. G. 2005, *ApJ*, 630, 1133, doi: [10.1086/432047](https://doi.org/10.1086/432047)
- Reeves, K. K., Freed, M. S., McKenzie, D. E., & Savage, S. L. 2017, *ApJ*, 836, 55, doi: [10.3847/1538-4357/836/1/55](https://doi.org/10.3847/1538-4357/836/1/55)
- Reeves, K. K., & Golub, L. 2011, *ApJL*, 727, L52, doi: [10.1088/2041-8205/727/2/L52](https://doi.org/10.1088/2041-8205/727/2/L52)
- Reeves, K. K., Linker, J. A., Mikić, Z., & Forbes, T. G. 2010, *ApJ*, 721, 1547, doi: [10.1088/0004-637X/721/2/1547](https://doi.org/10.1088/0004-637X/721/2/1547)
- Reeves, K. K., Seaton, D. B., & Forbes, T. G. 2008, *ApJ*, 675, 868, doi: [10.1086/526336](https://doi.org/10.1086/526336)
- Reeves, K. K., Török, T., Mikić, Z., Linker, J., & Murphy, N. A. 2019, *ApJ*, 887, 103, doi: [10.3847/1538-4357/ab4ce8](https://doi.org/10.3847/1538-4357/ab4ce8)
- Reznikova, V. E., & Shibasaki, K. 2011, *A&A*, 525, A112, doi: [10.1051/0004-6361/201015600](https://doi.org/10.1051/0004-6361/201015600)
- Savage, S. L., Holman, G., Reeves, K. K., et al. 2012, *ApJ*, 754, 13, doi: [10.1088/0004-637X/754/1/13](https://doi.org/10.1088/0004-637X/754/1/13)
- Savage, S. L., & McKenzie, D. E. 2011, *ApJ*, 730, 98, doi: [10.1088/0004-637X/730/2/98](https://doi.org/10.1088/0004-637X/730/2/98)
- Savage, S. L., McKenzie, D. E., Reeves, K. K., Forbes, T. G., & Longcope, D. W. 2010, *ApJ*, 722, 329, doi: [10.1088/0004-637X/722/1/329](https://doi.org/10.1088/0004-637X/722/1/329)
- Seaton, D. B., & Darnel, J. M. 2018, *ApJL*, 852, L9, doi: [10.3847/2041-8213/aaa28e](https://doi.org/10.3847/2041-8213/aaa28e)
- Seaton, D. B., & Forbes, T. G. 2009, *ApJ*, 701, 348, doi: [10.1088/0004-637X/701/1/348](https://doi.org/10.1088/0004-637X/701/1/348)
- Shen, C., Kong, X., Guo, F., Raymond, J. C., & Chen, B. 2018, *ApJ*, 869, 116, doi: [10.3847/1538-4357/aaeed3](https://doi.org/10.3847/1538-4357/aaeed3)
- Shibata, K., Nakamura, T., Matsumoto, T., et al. 2007, *Science*, 318, 1591, doi: [10.1126/science.1146708](https://doi.org/10.1126/science.1146708)
- Smith, D. M., Lin, R. P., Turin, P., et al. 2002, *SoPh*, 210, 33, doi: [10.1023/A:1022400716414](https://doi.org/10.1023/A:1022400716414)
- Somov, B. V., & Kosugi, T. 1997, *ApJ*, 485, 859, doi: [10.1086/304449](https://doi.org/10.1086/304449)
- Sturrock, P. A. 1966, *Nature*, 211, 695, doi: [10.1038/211695a0](https://doi.org/10.1038/211695a0)
- Su, Y., Veronig, A. M., Holman, G. D., et al. 2013, *Nature Physics*, 9, 489, doi: [10.1038/nphys2675](https://doi.org/10.1038/nphys2675)



- Sun, J. Q., Cheng, X., Ding, M. D., et al. 2015, *Nature Communications*, 6, 7598, doi: [10.1038/ncomms8598](https://doi.org/10.1038/ncomms8598)
- Sweet, P. A. 1958, in *IAU Symposium*, Vol. 6, *Electromagnetic Phenomena in Cosmical Physics*, ed. B. Lehnert, 123
- Takasao, S., Asai, A., Isobe, H., & Shibata, K. 2012, *ApJL*, 745, L6, doi: [10.1088/2041-8205/745/1/L6](https://doi.org/10.1088/2041-8205/745/1/L6)
- . 2016, *ApJ*, 828, 103, doi: [10.3847/0004-637X/828/2/103](https://doi.org/10.3847/0004-637X/828/2/103)
- Takasao, S., Matsumoto, T., Nakamura, N., & Shibata, K. 2015, *ApJ*, 805, 135, doi: [10.1088/0004-637X/805/2/135](https://doi.org/10.1088/0004-637X/805/2/135)
- Takasao, S., & Shibata, K. 2016, *ApJ*, 823, 150, doi: [10.3847/0004-637X/823/2/150](https://doi.org/10.3847/0004-637X/823/2/150)
- Tsuneta, S., & Naito, T. 1998, *ApJL*, 495, L67, doi: [10.1086/311207](https://doi.org/10.1086/311207)
- Veronig, A. M., Karlický, M., Vršnak, B., et al. 2006, *A&A*, 446, 675, doi: [10.1051/0004-6361:20053112](https://doi.org/10.1051/0004-6361:20053112)
- Veronig, A. M., Podladchikova, T., Dissauer, K., et al. 2018, *ApJ*, 868, 107, doi: [10.3847/1538-4357/aacac5](https://doi.org/10.3847/1538-4357/aacac5)
- Warren, H. P., Brooks, D. H., Ugarte-Urra, I., et al. 2018, *ApJ*, 854, 122, doi: [10.3847/1538-4357/aaa9b8](https://doi.org/10.3847/1538-4357/aaa9b8)
- Weber, M. A., Deluca, E. E., Golub, L., & Sette, A. L. 2004, in *IAU Symposium*, Vol. 223, *Multi-Wavelength Investigations of Solar Activity*, ed. A. V. Stepanov, E. E. Benevolenskaya, & A. G. Kosovichev (Cambridge University Press), 321–328, doi: [10.1017/S1743921304006088](https://doi.org/10.1017/S1743921304006088)
- Yan, X. L., Yang, L. H., Xue, Z. K., et al. 2018, *ApJL*, 853, L18, doi: [10.3847/2041-8213/aaa6c2](https://doi.org/10.3847/2041-8213/aaa6c2)
- Zeng, Z., Chen, B., Ji, H., Goode, P. R., & Cao, W. 2016, *ApJL*, 819, L3, doi: [10.3847/2041-8205/819/1/L3](https://doi.org/10.3847/2041-8205/819/1/L3)
- Zhu, C., Liu, R., Alexander, D., & McAteer, R. T. J. 2016, *ApJL*, 821, L29, doi: [10.3847/2041-8205/821/2/L29](https://doi.org/10.3847/2041-8205/821/2/L29)